Free Infragravity Waves in the North Sea

Rijnsdorp, Dirk P.; Reniers, Ad J.H.M.; Zijlema, Marcel

Important note
To cite this publication, please use the final published version (if applicable).
Please check the document version above.

Free Infragravity Waves in the North Sea

Dirk P. Rijnsdorp[1] , **Ad J. H. M. Reniers[1]** , and **Marcel Zijlema[1]**

[1]Environmental Fluid Mechanics Section, Department of Hydraulic Engineering, Faculty of Civil Engineering and Geosciences, Delft University of Technology, Delft, The Netherlands

Abstract Infragravity waves are low-frequency surface waves that can impact a variety of nearshore and oceanic processes. Recent measurements in the North Sea showed that significant bursts of infragravity energy occurred during storm events. Using a spectral wave model, we show that a substantial part of this energy was radiated from distant shorelines where it was generated by the incident sea-swell waves. These radiated infragravity waves can cross the North Sea basin and reach distant shorelines. The origin of the infragravity wave energy varied between the different storms, and particularly depends on where largest sea-swell waves made landfall. Along the coastlines of the North Sea, shoreward directed infragravity waves that originate from a remote source were non-negligible during storm events. This suggests that radiated infragravity waves can potentially contribute to coastal dynamics and hazards away from their region of generation.

Plain Language Summary Infragravity waves are long period surface waves that are small in the ocean but much larger in the shallow waters closer to the coast. In coastal regions, they are known to affect coastal safety assessments as they can, for example, impact the overtopping of coastal structures, enhance the erosion of dunes, and trigger the resonance of harbors. Recent observations in the North Sea showed that large infragravity waves occurred during storm events. By analyzing the measurements and using a wave model, we have shown that a substantial part of these waves was not generated locally but originated from distant shorelines. At such a distant shoreline, infragravity waves were generated by the breaking of sea-swell waves at the beach. After generation, the infragravity waves radiate into the North Sea, and modeling shows that they are able to cross the North Sea basin and reach distant shorelines. This study suggests that these radiated infragravity waves can be non-negligible along the borders of North Sea during storm events, and may contribute to coastal dynamics and nearshore hazards away from their region of generation.

1. Introduction

Infragravity (IG) waves are long period surface gravity waves with typical frequencies ranging between 0.005 and 0.05 Hz. They are typically small in oceanic waters where they have heights of $\mathcal{O}(\text{cm})$ (e.g., Aucan & Ardhuin, 2013; Webb et al., 1991), but can reach heights up to $\mathcal{O}(\text{m})$ in shallow water during severe weather events (e.g., Matsuba et al., 2020; Sheremet et al., 2014). In the past decades it has been well established that IG waves contribute to various nearshore processes, such as nearshore hydrodynamics (e.g., Guza & Thornton, 1985; Henderson & Bowen, 2002; Pomeroy et al., 2012), sediment transport (e.g., Aagaard & Greenwood, 1994; de Bakker et al., 2016), and erosion of beaches and dunes (e.g., Russell, 1993; Van Thiel de Vries et al., 2008). Associated with their longer periods, they can also trigger harbor seiches (e.g., Bowers, 1977; Cuomo & Guza, 2017; Okihiro et al., 1993; Thotagamuwage & Pattiaratchi, 2014) and excite large motions of moored vessels (e.g., Van der Molen et al., 2006, 2016). Despite their relative small amplitude in deeper water, they have been found to be the source of seismic hum (e.g., Ardhuin et al., 2015; Rhie & Romanowicz, 2006; Webb, 2007) and may impact the integrity of ice-shelves in polar regions (e.g., Bromirski et al., 2010, 2015).

IG waves are generally considered to be generated in the nearshore by interactions among wind-generated (sea-swell) surface gravity waves (e.g., Hasselmann, 1962; Longuet-Higgins & Stewart, 1962), see Bertin et al. (2018) for a recent review. These interactions are depth-dependant and only become significant (i.e., approach resonance) in shallow water. As a result, IG waves that are locally forced by the sea-swell waves (generally referred to as bound IG waves) are negligible in deep water. In the nearshore, the nonlinear
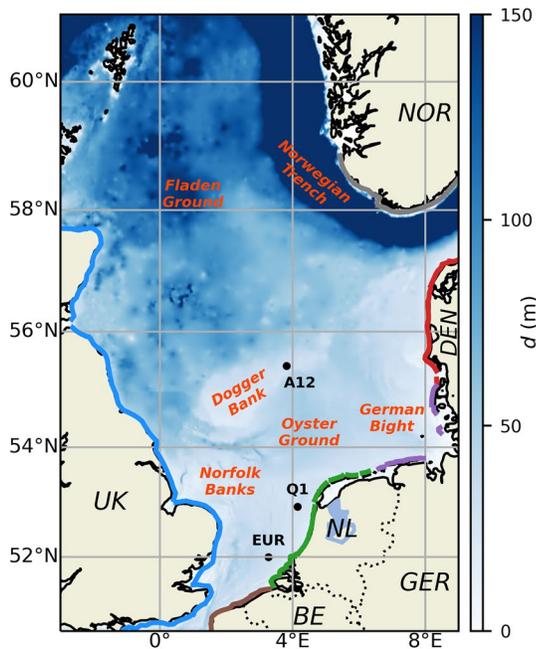
Figure 1. Bathymetry of the North Sea. Several geographic locations in the North Sea are indicated by the red labels. The markers indicate the three measurement stations (A12, Q1, and EUR). The colored lines indicate the locations along which the free infragravity source was imposed in the SWAN model, with the color indicating the corresponding country (blue: UK, brown: BE and FR, green: NL, purple: GER, red: DEN, gray: NOR).

interactions are (near) resonant and combined with other surf-zone generation mechanisms (such as the time-varying breakpoint, Symonds et al. (1982)) result in a substantial transfer of energy from the sea-swell to the IG frequencies. After (partial) reflection at the shoreline (e.g., Battjes et al., 2004; De Bakker et al., 2014; Van Dongeren et al., 2007), free infragravity (FIG) waves that are no longer bound to their forcing radiate seaward (e.g., Herbers, Elgar, & Guza, 1995; Herbers, Elgar, Guza, & O'Reilly, 1995). FIG energy levels reduce as the waves de-shoal in progressively deeper water and they can also become trapped in coastal waters and on the shelf due to refraction (e.g., Gallagher, 1971; Herbers, Elgar, & Guza, 1995; Munk et al., 1964; Okihiro et al., 1992), limiting their radiation into the open ocean (e.g., Webb et al., 1991; Smit et al., 2018). Nonetheless, part of the FIG energy can propagate beyond the shelf break and cross ocean basins (e.g., Crawford et al., 2015; Rawat et al., 2014; Smit et al., 2018; Webb et al., 1991).

Other deep water infragravity generation mechanics have also been proposed, such as atmospheric forcing by wind speed fluctuations (de Jong & Battjes, 2004; Vrećica et al., 2019) and IG-tidal interactions (Sugioka et al., 2010). By linking the arrival of FIG waves at oceanic sites to the landfall of energetic sea-swell waves at distant coastal regions, most deep water observations of IG energy have been explained by radiation of FIG waves at distant shorelines (e.g., Bogiatzis et al., 2020; Godin et al., 2014; Harmon et al., 2012; Neale et al., 2015; Tonegawa et al., 2018). Coastal regions with a narrow shelf that are subject to energetic sea-swell waves are generally believed to be a major radiator of FIG waves, although details regarding the dependence of FIG radiation on environmental conditions such as the sea state (e.g., the directional spreading and incident angles of sea-swell waves) and the coastal morphology is less well understood (Crawford et al., 2015; Smit et al., 2018). Beyond the world's oceans, the main contributors to IG energy and the role of radiated FIG waves in less explored regions such as inland and marginal seas remains largely unknown.

In this work, we study the temporal and spatial variability of IG energy in the North Sea during several energetic storm events. Recent analysis of measurements obtained between 2010 and 2018 at several stations in intermediate water depths (approx. 30 m) of the southern North Sea showed the occurrence of significant bursts of IG energy during storm events (Reniers et al., 2021). Only part of this energy could be attributed to bound IG waves that were excited by the local forcing from sea-swell waves (elaborated upon in Section 2.1). As a result, the source and origin of a substantial part of the observed IG energy remained unclear. The objective of this paper is to understand the dominant source and origin of this FIG energy for four of the most severe storm events in the observational record. We use the spectral wave model SWAN (Booij et al., 1999) extended with an empirical source of FIG energy along the shoreline (Ardhuin et al., 2014) to determine the contribution from FIG radiated from the coastlines bordering the North Sea (described in Section 2). Model-data comparisons at the three available measurement stations show that most of the FIG energy can be explained by radiation from distant shorelines (Section 3). In Section 3.4, the model results are further analyzed to gain insight into the onshore component of the FIG energy along the coastlines of the southern North Sea. This is followed by a discussion (Section 4) and the main conclusions of this work (Section 5).

2. Methods

2.1. Observations

Concurrent sea-swell and infragravity wave data were collected between 2010 and 2018 at three stations in intermediate water depths (approximately 30 m) of the southern North Sea (Figure 1). At these stations, a step gauge or radar combined with a wave buoy provided measurements of the sea-swell and infragravity waves. Both surface elevation spectra at sea and swell frequencies ($0.04 < f < 0.5$ Hz) and continuous

low-passed time-series of the surface elevation ($f < 0.025$) were stored (measured by the step gauge or radar). The sea-swell frequency spectra were combined with a directional distribution measured by the wave buoy to provide hourly estimates of directional sea-swell spectra. Hourly estimates of the infragravity wave frequency spectra (with $\Delta f = 0.0025$ Hz resolution) were obtained from the low-passed surface elevation time-series, which were sub-sampled at a 12.5 s time interval to limit data transfers to the shore. As a result of the processing, the infragravity wave spectra were only reliable at lower IG frequencies ($0.005 - 0.01$ Hz) and the higher IG frequencies ($0.01 - 0.04$ Hz) had to be excluded from the analysis (see Reniers et al. (2021) for more details).

At the intermediate water depths of the measurement stations, both FIG and bound IG waves (locally forced by the sea-swell waves) may contribute to energy at the IG frequencies. The contribution by bound IG waves to the energy density at the infragravity wave frequencies was estimated based on the measured directional sea-swell spectra using the second-order equilibrium theory of Hasselmann (1962) (refer to Reniers et al. (2021) for more details). The contribution from FIG waves was subsequently estimated by subtracting the predicted bound IG spectrum $E_b(f)$ from the measured IG spectrum $E(f)$. The FIG wave height H_{FIG} was computed by integrating the resulting spectrum over the IG frequency band,

$$H_{FIG} = 4\sqrt{\int_{0.005\text{Hz}}^{0.01\text{Hz}} \big(E(f) - E_b(f)\big)\mathrm{d}f} \tag{1}$$

2.2. Model

The spectral wave model SWAN was used to simulate the temporal and spatial evolution of FIG waves that were radiated from the shorelines bordering the North Sea. To account for the radiation of FIG waves from the shoreline, the SWAN model was extended with an empirical source of FIG energy following the approach of Ardhuin et al. (2014). The empirical source is based on a parametrization that prescribes the bulk IG wave height based on local sea-swell wave parameters (taken seaward from the surf-zone). This parametrization provided a good correlation at several locations in moderate to deep water (Ardhuin et al., 2014). Combined with an empirical spectral shape and isotropic directional distribution, the FIG source is given by,

$$E(f,\theta) = 1.2\alpha_1^2 \frac{kg^2}{c_g 2\pi f}\left(\frac{1}{4}H_{m0}T_{m0,-2}^2\right)^2 \times \frac{1}{\Delta_f}\big(\min(1.,0.015/f)\big)^{1.5} \times \frac{1}{2\pi}, \tag{2}$$

in which f is the wave frequency, k is the wave number, c_g is the group velocity, and Δ_f ensures that the frequency distribution integrates to 1. H_{m0} is the sea-swell significant wave height, $T_{m0,-2}$ is a sea-swell mean wave period, and α_1 is a (dimensional) calibration parameter. The source term can be imposed along waters of variable depth as the term $kg^2/c_g 2\pi f$ accounts for the shoaling of a directional broad wave spectrum (Ardhuin et al., 2014).

The IG source term was implemented as part of the obstacle functionality in SWAN, by which a line can be specified along which FIG energy should be radiated. In this work, we impose the IG source at intermediate water depths (≈ 15 m) along the major coastlines that face the southern North Sea (see Figure 1). In regions with complex shorelines, such as the Scheldt estuary and the Wadden Sea, the source was occasionally located in waters of 10 m depth. In regions with steep and irregular coastlines (e.g., along the Norwegian coast), the source term was located in water depths of ≈ 20 m.

The SWAN model was run in nonstationary mode with a spatial resolution of 0.025° and 0.0165° in longitudinal and latitudinal direction, respectively, a directional resolution of 8° and a time step of 1 h. Twenty-five discrete frequencies with default logarithmic spacing were used to discretize the IG frequency band ($0.005 \leq f \leq 0.05$ Hz). The spatial and directional resolutions were found to be sufficient based on sensitivity tests (A1). Reducing the time-step did not affect the model results (not shown). No additional source terms were included in the simulations, except for dissipation due to bottom friction using the JONSWAP formulation of Hasselmann et al. (1973). To understand the origin of the FIG waves in the North Sea, additional simulations were run with the same model-setup, but with a subset of coastlines radiating IG energy. Individual simulations were conducted with IG waves radiating from only the Belgium and French

(referred to as BE for brevity), Dutch (NL), German (GER), Danish (DEN), United Kingdom (UK), or Norwegian (NOR) coasts.

The sea-swell wave height H_{m0} and mean wave period $T_{m0,-1}$ (due to unavailability of $T_{m0,-2}$) of Equation 2 were obtained from the global ECMWF ERA5 reanalysis (Hersbach et al., 2020). These bulk wave parameter were available every hour at a 0.5° resolution, and were interpolated to the depths at which the IG source was specified. The α_1 parameter and the bottom friction coefficient were set based on a calibration study for a single storm event (storm Friedhelm) during which the majority of radiated FIG energy originated from the Danish coast (A2). Satisfactory results were obtained for $\alpha_1 = 18 \times 10^{-4}\,\text{s}^{-1}$, which is of the same order of magnitude as the values used in Ardhuin et al. (2014) and Rawat et al. (2014), in combination with a bottom friction coefficient of $\chi = 0.01\,\text{m}^2\text{s}^{-3}$. This bottom friction coefficient is lower than the default value $\chi = 0.038\,\text{m}^2\text{s}^{-3}$ typically used for sea-swell waves (e.g., Zijlema et al., 2012). To study the influence of bottom friction, additional simulations without bottom friction were conducted, for which the calibration study indicated optimal results for a slightly smaller α_1 value of $14.4 \times 10^{-4}\,\text{s}^{-1}$. In this work, a constant α_1 was used for all shorelines, and no attempt was made to optimize α_1 by varying it for different shorelines to account for differences between geographic regions (e.g., steep vs. mild bottom slopes) that may affect FIG radiation.

The SWAN model was used to hindcast four storm events that resulted in the largest observed H_{FIG} at the three measurement stations (storm Friedhelm, Dec 8–11, 2011; Xaver, Dec 5–8, 2013; Axel, Jan 4–5, 2017; and Egon, Jan 13–15, 2017). Directional spectra were outputted at the three measurement stations and along the shorelines bordering the southern North Sea (at approximately 20 m depth). The predicted H_{FIG} was computed by integrating the directional spectra from SWAN over all directions and the IG frequency band. When comparing model results with measurements, modeled FIG wave heights were integrated over the IG frequency band where measurements were available ($0.005 - 0.01$ Hz). With a frequency resolution of $\Delta f = 0.025$ Hz, only two data points were available in the observed IG spectra (see Section 2.1). The limited resolution of the observed spectra hampers a comparison between modeled and observed IG spectra. Therefore, this work is limited to studying temporal and spatial patterns of bulk IG wave heights.

2.3. Model-Data Comparison

We considered two statistical parameters to quantify the model-data agreement. The model skill was computed as,

$$\text{Skill} = 1 - \frac{\sqrt{\frac{1}{N}\sum_{i=1}^{N}(X_{\text{SWAN}}^{i} - X_{\text{obs}}^{i})^2}}{\sqrt{\frac{1}{N}\sum_{i=1}^{N}\left(X_{\text{obs}}^{i}\right)^2}}, \tag{3}$$

and the relative bias was computed as,

$$\text{RB} = \frac{\sum_{i=1}^{N}(X_{\text{SWAN}}^{i} - X_{\text{obs}}^{i})}{\sum_{i=1}^{N}X_{\text{obs}}^{i}}. \tag{4}$$

In these equations, X_{obs} indicates an observed value and X_{SWAN} is the corresponding modeled value.

3. Results

In the following, results are presented for the four considered storms events. The IG response at the three stations in the southern North Sea is first presented for the two largest storms (Section 3.1–3.2), during which free IG wave patterns in the North Sea were representative for all four considered storm events. This is followed by an overview of the FIG response for all four storm events, and an analysis of the role of bottom friction (Section 3.3). Subsequently, we use the model to gain a first insight in the potential coastal impact of remotely radiated FIG waves along the coastlines that border the North Sea (Section 3.4).
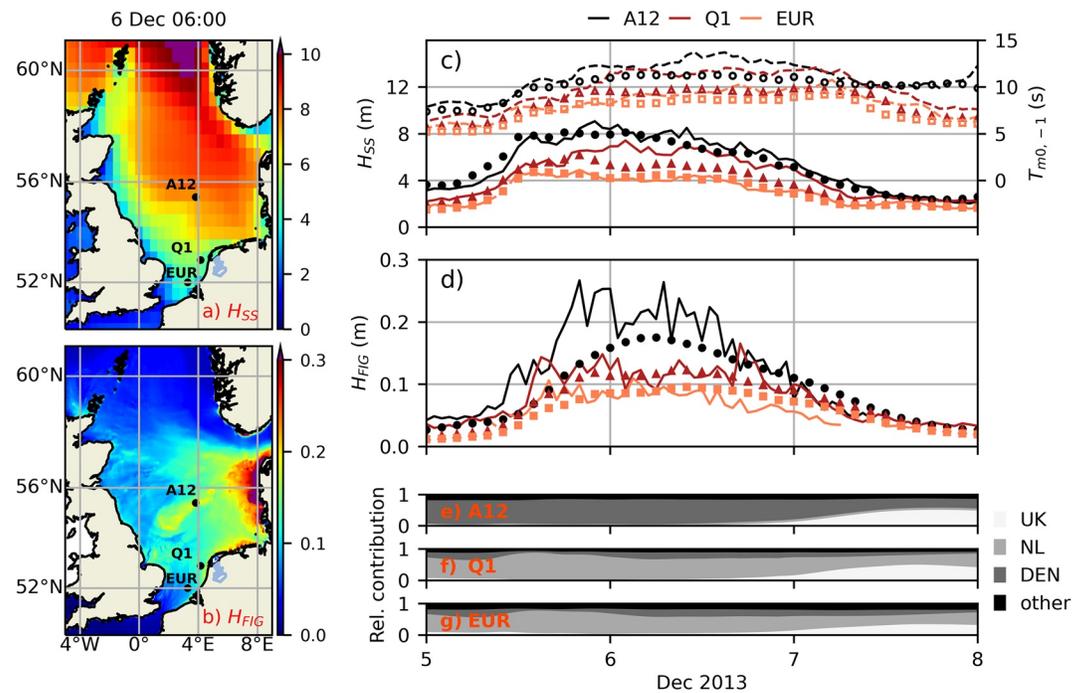
Figure 2. Sea-swell and infragravity wave conditions in the North Sea during storm Xaver (Dec 5–8, 2013). Snapshot of the instantaneous significant sea-swell (SS) wave height H_{SS} from the ERA5 reanalysis (panel a) and free infragravity (FIG) wave height H_{FIG} from the SWAN model (panel b) at 6 Dec 06:00 UTC. Observed (lines) and ERA5 (markers) time-series of H_{SS} (full line and filled markers, left axis) and $T_{m0,-1}$ (dashed lines and open markers, right axis) at three stations in the southern North Sea (A12, Q1 and EUR) (panel c). Observed (full lines) and SWAN (markers) FIG wave heights H_{FIG} at A12, Q1 and EUR (panel d). Relative contribution of different shorelines to the SWAN predicted FIG variance ($\propto H_{FIG}^2$) at the three stations (panel e–g).

3.1. Storm Xaver

In Dec 2013, a severe winter storm tracked from north of the UK toward the south of Norway and north of Denmark. Significant sea-swell wave heights H_{SS} at station A12 in the central North Sea reached 8 m with mean periods $T_{m0,-1}$ exceeding 10 s (Figure 2c), with largest sea-swell waves occurring in the northern part of the North Sea (e.g., Figure 2a). Storm Xaver produced the largest IG response in the observational record at A12, with FIG heights $H_{FIG} > 0.2$ m for approximately 24 h (Figure 2d). H_{FIG} was lower but still significant at stations Q1 and EUR, which are located further southward and in closer vicinity to the Dutch coast. During this storm event, FIG waves dominated the total IG variance as the contribution from bound IG waves was relatively small (see Figure 4 in Reniers et al. [2021]).

In accordance with the measurements (Figure 2d), the predicted FIG wave heights showed great spatial variability in the North Sea (e.g., near the peak of the storm at 6 Dec 06:00 UTC, Figure 2b). Largest H_{FIG} typically occurred near the Danish coast due to local radiation, and H_{FIG} decreased at an increasing distance away from the Danish coast. H_{FIG} was amplified by shoaling in regions of relatively shallow water, such as near the Dogger and Norfolk banks (refer to Figure 1 for the location of these geographic regions).

Predicted H_{FIG} captured the typical magnitude and trend of the observations at the three stations (Figure 2d). This indicates that the observed FIG levels can be partly explained by IG wave radiation from neighboring shorelines. The model failed to capture relatively large H_{FIG} at A12 prior to the peak of modeled H_{FIG} (02:00 UTC Dec 6). We will return to this model-data mismatch in Sections 3.3 and 4.

The model simulations further allow us to understand the temporal and spatial variability in H_{FIG} by considering the origin of the FIG energy. For the majority of the storm, the modeled H_{FIG} at A12 primarily originated from the Danish coast (Figure 2e), which can be explained by the occurrence of the largest sea-swell waves in the northern part of the North Sea (Figure 2a). At Q1 and EUR however, most of the modeled FIG
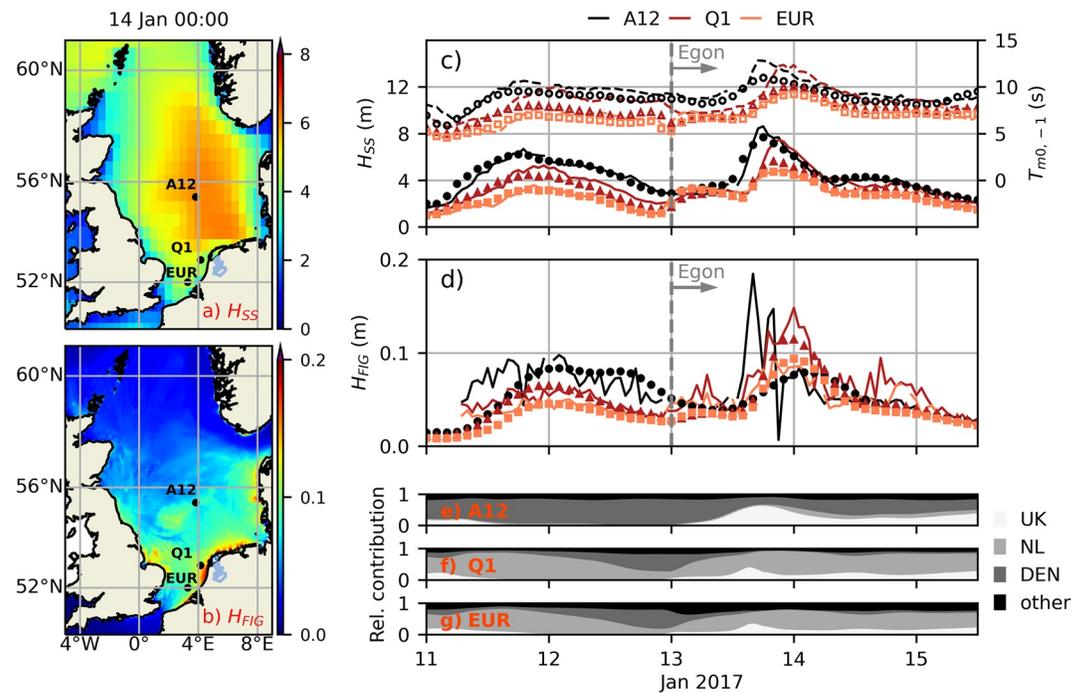
Figure 3. Sea-swell and infragravity wave conditions in the North Sea prior to (Jan 11–13, 2017) and during storm Egon (Jan 13–15, 2017). Refer to the caption of Figure 2 for further details.

variance originated from the Dutch coast (Figures 2f and 2g), with a smaller but non-negligible contribution from the Danish coast ($\approx 10 - 20\%$ of the FIG variance). This shows that FIG energy radiated from the Danish coast reached these stations in the southern North Sea, despite attenuation by refraction and bottom friction. We will return to the effect of bottom friction in Section 3.3.

3.2. Storm Egon

During storm Egon, large sea-swell waves occurred between Jan 13 and 15, with H_{SS} up to 8 m at A12, and with H_{SS} peaking at 5 m at EUR in the southern North Sea (Figure 3c). Bound IG wave heights contributed significantly to the IG energy at station A12 and Q1 during storm Egon (see Figure 6 in Reniers et al. [2021]). Nonetheless, bound waves contributions did not completely explain the IG energy, resulting in substantial free IG energy levels at all three measurement stations (Figure 3d). Storm Egon was preceded by another storm (Jan 11–13), with weaker but still significant waves ($H_{SS} > 4$ m at A12 and Q1). Between Jan 11 and 13, FIG patterns were comparable to storm Xaver with largest H_{FIG} at A12 and progressively smaller H_{FIG} toward the south at Q1 and EUR. During storm Egon (Jan 13–15) H_{FIG} showed remarkably different patterns. Prior to the peak of the storm (at approximately 21:00 UTC, Jan 13) H_{FIG} was largest at A12 and got progressively smaller at stations Q1 and EUR in the southern North Sea. Following the peak of the storm however, H_{FIG} was largest at Q1 and smallest at A12.

The model captured the typical magnitude of H_{FIG} at all three stations, except for large H_{FIG} at A12 prior to the peak of both storms (similar to the findings for storm Xaver). Notably, the model captured the general trends in H_{FIG} during storm Egon (Jan 13–15), including the observation that H_{FIG} at station Q1 and EUR exceeded H_{FIG} at A12 following the peak of storm Egon. The general agreement between the model and the observations indicates that a significant part of the IG energy can be attributed to the arrival of FIG waves that were radiated from nearby shorelines.

Given the satisfactory model-data comparison, we can use the model results to explain the different patterns in H_{FIG} between the two storm events (Figures 3e–3g). During the first storm (Jan 11–13) modeled H_{FIG} at A12 mainly originated from Denmark, whereas between Jan 13 and 15, H_{FIG} was primarily explained by contributions from Denmark and the UK. At Q1 and EUR, FIG radiation from the Dutch and Danish coast

including bottom friction ($\alpha_1 = 18.0 \times 10^{-4} \, s^{-1}$, $\chi = 0.01 \, m^2$)
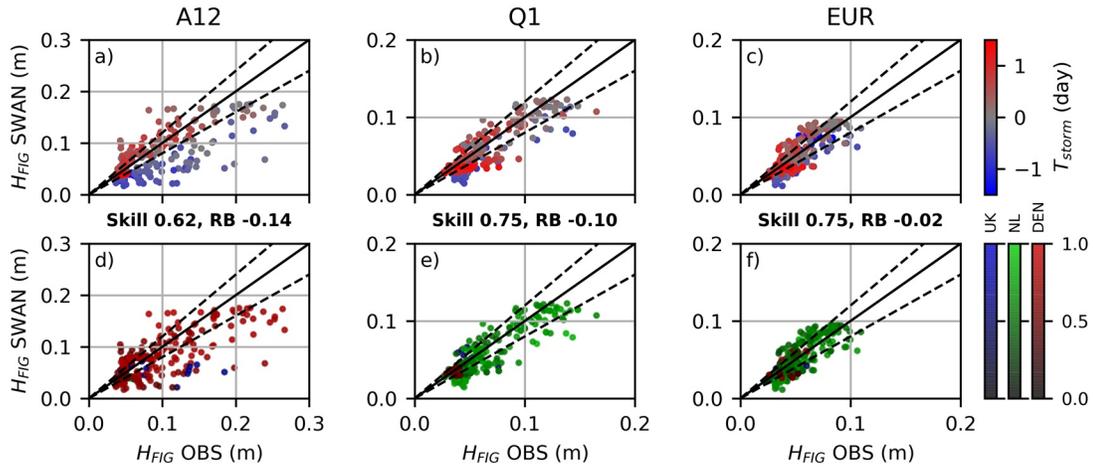
no bottom friction ($\alpha_1 = 14.4 \times 10^{-4} \, s^{-1}$, $\chi = 0. \, m^2$)
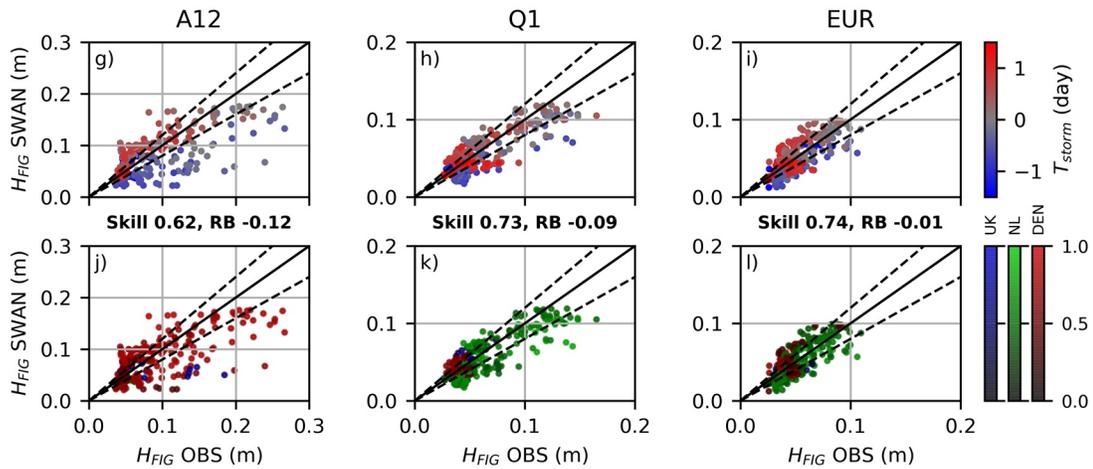
Figure 4. Scatter plot of the instantaneous observed (OBS) versus modeled (SWAN) FIG wave height H_{FIG} at station A12 (left panels), Q1 (middle panels) and EUR (right panels) for all four considered storm events. The top plots (panel a–f) show the modeling results including the effect of bottom friction, and the bottom plots (panel g–l) show the results excluding bottom friction. In panels (a–c) and (g–i), the marker color indicates the time relative to the approximate peak in the observed H_{FIG} at A12. In panels (d–f) and (j–l), the marker color indicates the region from which the majority of the IG variance ($\propto H_{FIG}^2$) originated. The color shading indicates the relative contribution of this region to the total IG variance, with darker colors indicative for significant contributions from multiple regions.

contributed to the FIG variance during the first storm (with the contribution from Denmark gradually increasing during the waning of the storm). In contrast, the FIG variance was primarily explained by radiation from the Dutch and UK coast during storm Egon. The modeling results thus suggest that the different patterns in H_{FIG} (largest H_{FIG} at A12 between Jan 11 and 13 and largest H_{FIG} at Q1 around Jan 14) were related to the storm trajectory and the spatial variability of the sea-swell waves. This resulted in stronger IG radiation from the Danish coast between Jan 11 and 13 due to a more northerly track of sea-swell waves, and stronger IG radiation along the shorelines of the southern North Sea (UK and NL) between Jan 13 and 15 due to a more south westerly track of sea-swell waves (see also the animation of the SS and FIG wave height in the Supporting Information S1).

3.3. All Storms and the Influence of Bottom Friction

Comparing the observed and modeled H_{FIG} at all stations for all considered storm events shows that the model (including bottom friction) generally reproduced the observations (Figure 4). The agreement was

best at Q1 and EUR, where the model Skill indicates that the model explained 75% of the variability in the FIG wave height (Figures 4b and 4c). At these stations, the model suggests that the FIG variance was typically dominated by radiation from the nearby Dutch coast (Figures 4e and 4f).

The agreement at A12 was poorer (Figure 4a), with a lower Skill and larger Relative Bias (RB) consistent with a typical under prediction of H_{FIG}. This under prediction at A12 occurred consistently at times prior to the peak of all four storms (blue markers in Figure 4a), as was observed previously for storm Xaver and Egon (Figures 2 and 3). We will return to this in Section 4. Near and following the peak of the storm (gray to red markers in Figure 4a), the model did capture H_{FIG}, showing that at these times the observed FIG waves originated from surrounding shorelines. At station A12, the modeled FIG variance was typically dominated by radiation from the Danish coast (Figure 4d).

To study the influence by bottom friction, the SWAN simulations were repeated excluding the bottom friction source term and a slightly lower α_1 value (to compensate for the absence of frictional dissipation). The influence of bottom friction on H_{FIG} is particularly notable at stations Q1 and EUR where it reduced the Danish contribution at times that significant IG variance originated from Denmark (compare Figures 4e and 4f with Figures 4k–4i). Including frictional dissipation resulted in a minor improvement of the overall model skill. These results indicate that bottom friction can provide some additional attenuation of FIG waves as they propagate through the relatively shallow North Sea basin. For the four storms considered, the bottom friction only led to noticeable additional attenuation at Q1 and EUR when the majority of FIG energy originated from the Danish coast.

3.4. Shoreward Directed Remotely Generated FIG Energy

The results in the previous subsections did not consider the full IG frequency band (due to measurement limitations) and focused on three stations in intermediate water depths of the southern North Sea. To gain insight into the potential magnitude of remotely generated FIG energy that is incident to the coast, two-dimensional spectra were outputted at approximately 20 m depth along the coastlines bordering the southern North Sea (the output locations were always located seaward of the generation line of the IG source term). The magnitude of the shoreward directed FIG wave height was computed by integrating the SWAN spectra over the full IG frequency band and the shoreward directed directional bins,

$$H_{FIG}^+ = 4\sqrt{\int_{0.005\,\mathrm{Hz}}^{0.05\,\mathrm{Hz}} \int_{\theta_p -90°}^{\theta_p +90°} E(f,\theta)\mathrm{d}\theta\mathrm{d}f}\,, \tag{5}$$

in which θ_p is the angle perpendicular to the shore. To exclude contributions from locally radiated FIG waves that are trapped by refraction, we excluded the local FIG source from the different subsets of simulations (e.g., when computing H_{FIG}^+ along the UK coast, the FIG forcing along the UK coastline was excluded from the simulations). This implies that H_{FIG}^+ only includes the contribution from FIG waves that were radiated at distant (e.g., trans-basin) shorelines.

Figure 5 shows the maximum H_{FIG}^+ with a remote origin at approximately 20 m water depth that occurred during each of the four storms (top to bottom panels) along the UK coastline (left panels) and the coastline between Belgium and Denmark (right panels). The maximum H_{FIG}^+ shows a similar variability along the UK coastline for the four storm events, with overall largest levels between the 53-54° latitude mark (the coastline facing the Norfolk Banks, see Figure 1), typically lower levels toward the south, and relatively constant values north of 54° latitude (left panels of Figure 5). The origin of this remotely radiated FIG energy varied in space and differed per storm. In the north, the maximum H_{FIG}^+ mainly originated from Denmark for all four storms. In contrast, the contribution from the nearby Dutch and Belgium coast progressively increased toward the south. Nonetheless, the Danish contribution was still significant during storm Friedhelm and Xaver (Figures 5a and 5c, respectively) during which largest sea-swell waves made landfall along the Danish coast.

The maximum H_{FIG}^+ also shows a strong spatial variation along the coastlines between Belgium and Denmark (right panel Figure 5). The origin of the maximum H_{FIG}^+ varied strongly in space and differed per storm. During storm Friedhelm and Xaver, the maximum H_{FIG}^+ along the Belgian to German coast mainly
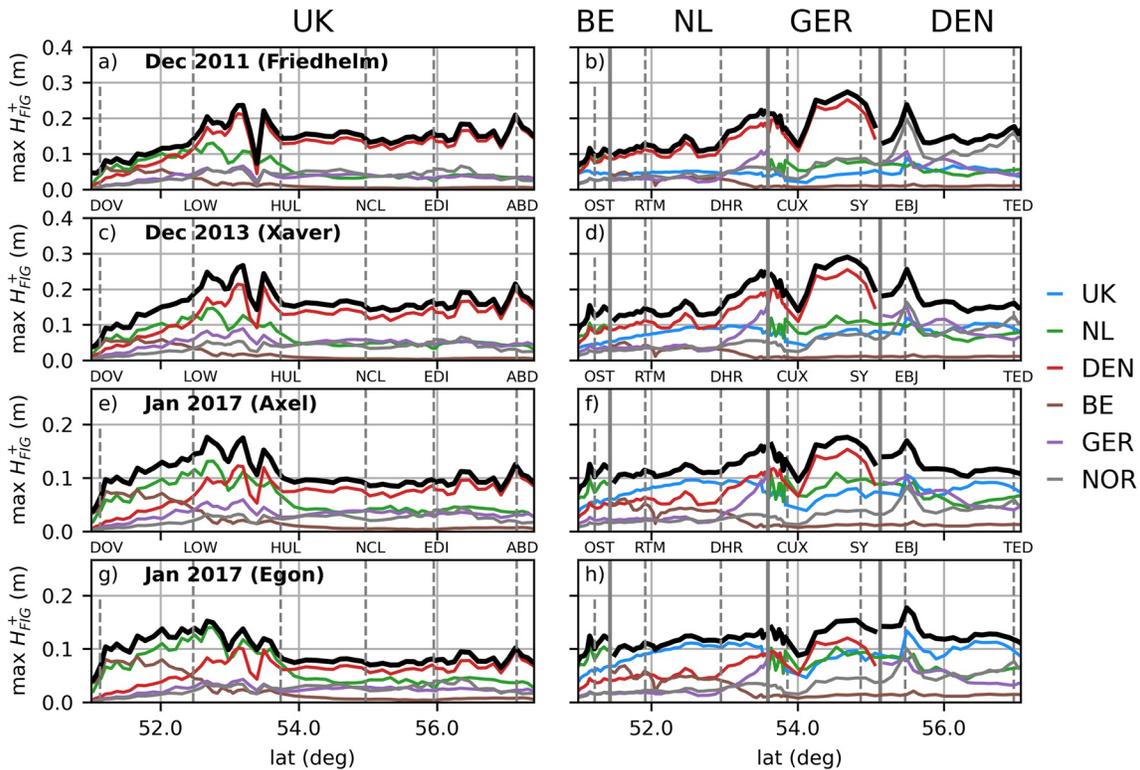
Figure 5. Maximum of the SWAN modeled (including bottom friction) shoreward directed FIG wave height H_{FIG}^+ with a remote source (black line) during individual storm events along the Eastern UK coastline (left panels) and the coastlines between Belgium and Denmark (right panels) at approximately 20 m water depth. The colored lines indicate the H_{FIG}^+ that was radiated from different national regions (as indicated by the legend). In the right panels, the thick gray vertical lines indicate the approximate border of the different national regions. The vertical dashed lines indicate several geographical locations along the coastline. Left panels: DOV (Dover), LOW (Lowestoft), Hul (Hull), NCL (Newcastle), EDI (Edingburgh), ABD (Aberdeen); Right panels: OST (Ostend), RTM (Rotterdam), DHR (Den Helder), CUX (Cuxhaven), SY (Sylt), EBJ (Esbjerg), TED (Thisted).

originated from Denmark (Figures 5b and 5d, respectively). In contrast, during storm Axel and especially Egon the UK coast contributed significantly to the maximum H_{FIG}^+ along this stretch of coast (Figures 5f and 5g, respectively). These findings demonstrate that, during these four storm events, the shoreward directed component of FIG waves that were radiated at distant coasts was non-negligible along the shorelines bordering the North Sea.

4. Discussion

We used a spectral wave model to explain observations of IG waves in the southern North Sea during four of the largest storm events between 2010 and 2018. The model relies on an empirical source of FIG energy along the shoreline (depending on bulk sea-swell parameters and a calibration parameter α_1) that parametrizes the highly nonlinear dynamics that govern the excitation of IG waves by the shoaling and breaking of sea-swell waves in coastal waters and the subsequent reflection at the shoreline. Despite the highly empirical approach to capture the radiation of FIG along the shoreline, the model was able to explain up to 75% of the variability in the observed FIG wave height.

This source term does however not account for various characteristics of the sea-swell wavefield that are known to influence the nearshore generation of IG waves (beyond the dependence on the sea-swell wave height and mean period). For example, the nearshore excitation and reflection of IG waves is known to depend on the directional properties of the sea-swell waves (e.g., Herbers et al., 1994; Herbers, Elgar, Guza, & O'Reilly, 1995; Okihiro et al., 1992). Furthermore, the model-data agreement strongly depends on the α_1 calibration parameter that accounts for differences in FIG radiation under the same sea-swell conditions

due to, for example, spatial variations in the beach morphology. Variations in α_1 are likely strongly related to the nearshore beach morphology. The nearshore reflection of IG waves (and thus FIG wave radiation) is well known to depend on the normalised beach slope (Van Dongeren et al., 2007), with stronger reflections at relative steep beaches (with respect to the IG wave length) compared to relatively moderate or mildly sloping beaches (e.g., De Bakker et al., 2014; Guedes et al., 2013; Inch et al., 2017). IG wave reflections can also exhibit a temporal variation due to changes in the beach slope during a tidal cycle (e.g., Bertin et al., 2020; Okihiro & Guza, 1995; Thomson et al., 2006). Furthermore, enhanced IG reflections were observed at a mildly sloping beach during a significant storm event and were explained by energy transfers to lower IG frequencies (Bertin et al., 2020). The nearshore generation and reflection of IG waves (and thus FIG wave radiation) can thus vary in space and time depending on the coastal morphology and sea-swell characteristics.

Surprisingly, a constant α_1 for all coastlines was sufficient to obtain a reasonable model-data agreement, even though (Ardhuin et al., 2014) found that α_1 can vary by up to a factor two for different coastlines (consistent with the spatial and temporal variation of IG radiation discussed above). The reasonable agreement for a constant α_1 could be related to the limited IG frequency band ($0.005 < f < 0.01$ Hz) that was considered in this study due to measurement limitations. Such low frequency IG waves have been observed to significantly reflect at both relatively steep and milder beach slopes (e.g., De Bakker et al., 2014; Guedes et al., 2013; Inch et al., 2017). As a result, the radiation of low frequency IG waves could exhibit a weaker dependence on the nearshore coastal geometry compared to higher frequency IG waves.

Discrepancies between the model results and the observations could be related to short-comings in the IG source term, measurement inaccuracies, the exclusion of other FIG generation mechanisms, or a combination thereof. Using a spatially and temporal varying α_1 to account for variations in FIG radiation is beyond the scope of the present work, but could explain some of the discrepancies between the modeled and observed H_{FIG}. For example, the observed H_{FIG} shows somewhat of a temporal modulation with a period of approximately 12 h at A12 during storm Xaver (Figure 2d). The time-scale of this modulation is consistent with the semi-diurnal tide that occurs in the North Sea. This temporal modulation of H_{FIG} could thus be related to a tidal modulation in the FIG radiation from the surrounding beaches.

However, a spatially and temporal varying α_1 will unlikely be able to explain all model-data discrepancies. In particular, H_{FIG} was consistently under predicted at station A12 (located on the north-eastern slope of the Doggers Bank, see Figure 1) during the onset of all four storms (Figure 4a). At times of this under prediction, significant sea-swell waves approached A12 from the north during all four storm events. Significant sea-swell waves did not yet reach adjacent coast at this time, resulting in weak radiation of FIG wave energy from surrounding coasts (see the animations in the Supporting Information S1). This suggests that the unexplained FIG energy during the onset of the storms cannot likely be completely explained by FIG radiation from surrounding beaches.

Previous studies in deep water could directly relate observed energy levels at IG frequencies to FIG waves due to negligible contributions from bound IG waves (e.g., Ardhuin et al., 2014; Rawat et al., 2014; Smit et al., 2018). In the intermediate water depths of the the North Sea however, observed FIG energy levels depend directly on the estimates of the bound IG energy levels (through Equation 1) as nonlinear wave-interactions were non-negligible. The bound IG spectra E_b were estimated from observed directional wave spectra using second-order equilibrium theory (Hasselmann, 1962). As a result, estimates of E_b are affected by possible inaccuracies in the directional distribution measured by the wave buoys and by the potential violation of the assumptions underpinning second-order theory (i.e., a stationary and spatially homogeneous weakly nonlinear wavefield). Due to unavailability of surface elevation and/or pressure time-series of the sea-swell waves we could not estimate E_b using bispectral analysis (following the approach of Herbers et al. (1994)). We therefore lack insight in potential inaccuracies from the measured directional distributions. To assess whether the assumption of weak nonlinearity was violated we quantified the wave non-linearity using the Ursell number, $U_r = (a/d)/(kd)^2$ (in which d is the local water depth, and we estimated the wave amplitude as $a = H_{SS}/2$ and the wave number k using the linear dispersion relationship based on $T_{m0,-1}$). At station A12, U_r peaked around 0.15, indicating that the assumption of weak non-linearity was not violated. Furthermore, the assumption of spatial homogeneity was not likely violated as the bottom topography does not vary significantly near station A12 (with bottom slopes of $\mathcal{O}(1/1000)$). However, temporal

variations in the sea-swell wavefield were significant during the onset of the storm when the first significant sea-swell waves arrived at A12, but the impact of this on E_b estimates is unclear.

Based on the current modeling and with the available measurement data we cannot establish the reason for the under prediction of H_{FIG} at A12 during the onset of the four storms. Further research is required to understand this model-data mismatch, and to study whether other physical mechanisms could have been responsible for the excitation of the unexplained FIG wave energy at station A12.

5. Conclusions

In-situ observations at three measurement stations in the southern North Sea revealed the occurrence of substantial bursts of free infragravity wave energy during four significant storm events. A spectral wave model that accounts for the radiation of FIG waves from adjacent beaches was able to explain up to 75% of the observed variability in the FIG wave height. The model captured the typical magnitude and temporal variation of the FIG wave height at the three measurement stations. Although the model failed to explain significant FIG energy levels that occurred prior to the peak of storms at the measurement site in the central North Sea (suggesting that other processes also contributed to FIG energy at this location), the overall model-data agreement suggests that a significant fraction of the FIG energy levels in the southern North Sea originated from distant shorelines. These results are in accordance with previous studies on the shelf or near the shelf break (e.g., Harmon et al., 2012; Smit et al., 2018; Tonegawa et al., 2018) and in the deep ocean (e.g., Bogiatzis et al., 2020; Crawford et al., 2015; Neale et al., 2015; Rawat et al., 2014) that linked significant energy at IG frequencies to radiation of FIG from distant shorelines.

The origin of the FIG energy in the North Sea was found to depend on the storm characteristics, and in particular on where large sea-swell waves made landfall. The model suggests that radiated FIG energy was able to cross the North Sea basin and reach neighboring shorelines with minor additional attenuation due to bottom friction. Along the coastlines at approximately 20 m depth, the model showed that during storms the shoreward directed component of the remotely radiated FIG waves were non-negligible. This shows that radiated FIG waves can potentially impact the coastal environment in the North Sea away from their region of generation, and influence processes like flooding, dune erosion, and seiching of harbors.

Appendix A: Model Sensitivity Study and Calibration

A1. Sensitivity Study (Spatial and Directional Resolution)

A sensitivity study was conducted to determine the optimal spatial and directional resolution of the SWAN simulations. A stationary simulation (with the 1st order BSBT propagation scheme) was ran with all shore-lines along the North Sea radiating an equal amount of IG energy. The grid and directional resolution were varied and compared with a reference simulation. The reference simulation was run with the 2nd order SOR-DUP propagation scheme and with the finest considered spatial and directional resolution. The directional resolution was varied between $2° - 15°$ and the longitudinal grid resolution was varied between $0.01 - 0.05°$. The latitudinal resolution was kept as a constant fraction (≈ 1.5) of the longitudinal resolution. For each simulation, we compute the model skill (Equation 3) relative to the reference simulation for the free infra-gravity wave height H_{FIG} at the three measurement stations.

This sensitivity study showed that the model results were only weakly affected by the directional and grid resolution (Figure A1). Based on these results, the model simulations were conducted with a resolution of $0.025°$ in longitudinal and $0.0165°$ in latitudinal direction, and a directional resolution of $\Delta\theta = 8°$.

A2. Calibration Study (α_1 and χ)

Following the model sensitivity study, a calibration study was conducted to select the α_1 parameter of the infragravity source term, and the χ parameter of the JONSWAP friction formulation. For this purpose, we conducted a non-stationary simulation of storm Friedhelm. During storm Friedhelm, significant sea-swell waves mainly made landfall in Denmark, and modeled H_{FIG} in the North Sea were dominated by infra-
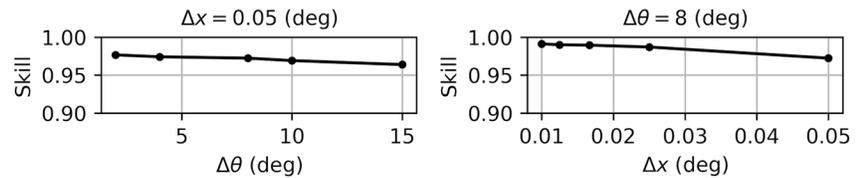
Figure A1. Model skill for a varying directional resolution ($\Delta\theta$) with a fixed grid resolution (with Δx the longitudinal resolution) (left panel), and for a varying grid resolution with a fixed directional resolution (right panel).

gravity waves radiated from the Danish coast. This allowed for a more straightforward model calibration compared to a storm during which H_{FIG} originated from multiple coastal sections.

First, we selected the α_1 parameter based on the model-data agreement at station A12 for the simulation without bottom friction. This resulted in $\alpha_1 = 14.4 \times 10^{-4}$ s^{-1}. Without friction, H_{FIG} is slightly over predicted at station EUR (Figure A2). Subsequently, we varied α_1 and χ to 1) match the predictions without bottom friction at A12, and 2) improve the model-data agreement at station EUR. This resulted in $\alpha_1 = 18 \times 10^{-4}$ s^{-1} and $\chi = 0.01$ m^2. As the model-data agreement with these model parameters was satisfactory for the other storms, we made no attempt to optimize the model results by calibrating α_1 for separate coastal sections.
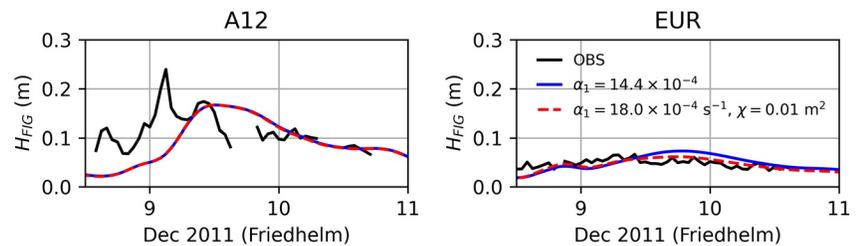
Figure A2. Observed (black line) and predicted (excluding friction, blue line; and including friction, dashed red line) free infragravity wave height H_{FIG} at station A12 (left panel) and station EUR (right panel) during storm Friedhelm.

Data Availability Statement

The ERA5 reanalysis is publicly available from the Climate Data Store of the Copernicus Climate Change Service (https://doi.org/10.24381/cds.adbb2d47). The measured infragravity wave data is available from the 4TU.ResearchData repository (https://doi.org/10.4121/13370123). The source code of the adapted SWAN model is also available from the 4TU.ResearchData repository (https://doi.org/10.4121/14754054.v1). The SWAN-DCSM model schematization (SWAN-DCSM-j15-v1) was kindly provided by Deltares and Rijkswaterstaat.

References

Aagaard, T., & Greenwood, B. (1994). Suspended sediment transport and the role of infragravity waves in a barred surf zone. *Marine Geology*, *118*(1–2), 23–48. https://doi.org/10.1016/0025-3227(94)90111-2

Ardhuin, F., Gualtieri, L., & Stutzmann, E. (2015). How ocean waves rock the Earth: Two mechanisms explain microseisms with periods 3 to 300s. *Geophysical Research Letters*, *42*(3), 765–772. https://doi.org/10.1002/2014GL062782

Ardhuin, F., Rawat, A., & Aucan, J. (2014). A numerical model for free infragravity waves: Definition and validation at regional and global scales. *Ocean Modelling*, *5*, 20–32. https://doi.org/10.1016/j.ocemod.2014.02.006

Aucan, J., & Ardhuin, F. (2013). Infragravity waves in the deep ocean: An upward revision. *Geophysical Research Letters*, *40*(13), 3435–3439. https://doi.org/10.1002/grl.50321

Battjes, J. A., Bakkenes, H. J., Janssen, T. T., & Van Dongeren, A. R. (2004). Shoaling of subharmonic gravity waves. *Journal of Geophysical Research*, *109*(C2). https://doi.org/10.1029/2003jc001863

Bertin, X., Bakker, A. d., Dongeren, A. v., Coco, G., André, G., Ardhuin, F., & Tissier, M. (2018). Infragravity waves: From driving mechanisms to impacts. *Earth-Science Reviews*, *1*. https://doi.org/10.1016/j.earscirev.2018.01.002

Bertin, X., Martins, K., de Bakker, A., Chataigner, T., Guérin, T., Coulombier, T., & de Viron, O. (2020). Energy transfers and reflection of infragravity waves at a dissipative beach under storm waves. *Journal of Geophysical Research: Oceans*, *125*(5), 1–18. https://doi.org/10.1029/2019JC015714

Bogiatzis, P., Karamitrou, A., Ward Neale, J., Harmon, N., Rychert, C. A., & Srokosz, M. (2020). Source regions of infragravity waves recorded at the bottom of the equatorial Atlantic Ocean, using OBS of the PI-LAB experiment. *Journal of Geophysical Research: Oceans*, *6*(6), 1–17. https://doi.org/10.1029/2019JC015430.125

Booij, N., Ris, R. C., & Holthuijsen, L. H. (1999). A third-generation wave model for coastal regions: 1. Model description and validation. *Journal of Geophysical Research*, *104*(C4), 7649–7666. https://doi.org/10.1029/98jc02622

Bowers, E. C. (1977). Harbour resonance due to set-down beneath wave groups. *Journal of Fluid Mechanics*, *79*(1), 71–92. https://doi.org/10.1017/S0022112077000044

Bromirski, P. D., Diez, A., Gerstoft, P., Stephen, R. A., Bolmer, T., Wiens, D. A., et al. (2015). Ross ice shelf vibrations. *Geophysical Research Letters*, *42*(18), 7589–7597. https://doi.org/10.1002/2015GL065284

Bromirski, P. D., Sergienko, O. V., & MacAyeal, D. R. (2010). Transoceanic infragravity waves impacting Antarctic ice shelves. *Geophysical Research Letters*, *1*(2). https://doi.org/10.1029/2009gl041488

Crawford, W., Ballu, V., Bertin, X., & Karpytchev, M. (2015). The sources of deep ocean infragravity waves observed in the North Atlantic Ocean. *Journal of Geophysical Research: Oceans*, *7*(7), 5120–5133. https://doi.org/10.1002/2014jc010657

Cuomo, G., & Guza, R. T. (2017). Infragravity seiches in a small harbor. *Journal of Waterway, Port, Coastal, and Ocean Engineering*, *143*(5), 04017032. https://doi.org/10.1061/(asce)ww.1943-5460.0000392

de Bakker, A. T., Brinkkemper, J. A., van der Steen, F., Tissier, M. F., & Ruessink, B. G. (2016). Cross-shore sand transport by infragravity waves as a function of beach steepness. *Journal of Geophysical Research: Earth Surface*, *121*(10), 1786–1799. https://doi.org/10.1002/2016JF003878

De Bakker, A. T. M., Tissier, M. F. S., & Ruessink, B. G. (2014). Shoreline dissipation of infragravity waves. *Continental Shelf Research*, *1*, 73–82. https://doi.org/10.1016/j.csr.2013.11.013

de Jong, M. P., & Battjes, J. A. (2004). Low-frequency sea waves generated by atmospheric convection cells. *Journal of Geophysical Research*, *109*(1), 1–18. https://doi.org/10.1029/2003jc001931

Gallagher, B. (1971). Generation of surf beat by non-linear wave interactions. *Journal of Fluid Mechanics*, *49*(1), 1–20. https://doi.org/10.1017/S0022112071001897

Godin, O. A., Zabotin, N. A., Sheehan, A. F., & Collins, J. A. (2014). Interferometry of infragravity waves off New Zealand. *Journal of Geophysical Research: Oceans*, *2*(2), 1103–1122. https://doi.org/10.1002/2013jc009395

Guedes, R. M. C., Bryan, K. R., & Coco, G. (2013). Observations of wave energy fluxes and swash motions on a low-sloping, dissipative beach. *Journal of Geophysical Research: Oceans*, *118*(7), 3651–3669. https://doi.org/10.1002/jgrc.20267

Guza, R. T., & Thornton, E. B. (1985). Observations of surf beat. *Journal of Geophysical Research*, *90*(C2), 3161–3172. https://doi.org/10.1029/jc090ic02p03161

Harmon, N., Henstock, T., Srokosz, M., Tilmann, F., Rietbrock, A., & Barton, P. (2012). Infragravity wave source regions determined from ambient noise correlation. *Geophysical Research Letters*, *39*(4). https://doi.org/10.1029/2011GL050414

Hasselmann, K. (1962). On the non-linear energy transfer in a gravity-wave spectrum: Part 1. General theory. *Journal of Fluid Mechanics*, *12*(4), 481–500. https://doi.org/10.1017/S0022112062000373

Hasselmann, K., Barnett, T. P., Bouws, E., Carlson, H., Cartwright, D. E., Enke, K., & Walden, H. (1973). Measurements of wind-wave growth and swell decay during the Joint North Sea Wave Project (JONSWAP). *Erganzungsheft zur Deutschen Hydrographischen Zeitschrift*, *A8*(12). https://hdl.handle.net/21.11116/0000-0007-DD3C-E

Henderson, S. M., & Bowen, A. J. (2002). Observations of surf beat forcing and dissipation. *Journal of Geophysical Research*, *107*(C11). https://doi.org/10.1029/2000jc000498

Herbers, T. H. C., Elgar, S., & Guza, R. T. (1994). Infragravity-Frequency (0.005–0.05 Hz) Motions on the Shelf. Part I: Forced Waves. *Journal of Physical Oceanography*, *24*(5), 917–927. https://doi.org/10.1175/1520-0485(1994)024⟨0917:IFHMOT⟩2.0.CO;2

Herbers, T. H. C., Elgar, S., & Guza, R. T. (1995). Generation and propagation of infragravity waves. *Journal of Geophysical Research*, *100*, 24863–24872. https://doi.org/10.1029/95JC02680

Herbers, T. H. C., Elgar, S., Guza, R. T., & O'Reilly, W. C. (1995). Infragravity-frequency (0.005–0.05 Hz) motions on the shelf. Part II: Free waves. *Journal of Physical Oceanography*, *25*(6), 1063–1079. https://doi.org/10.1175/1520-0485(1995)025<1063:ifhmot>2.0.co;2

Hersbach, H., Bell, B., Berrisford, P., Hirahara, S., Horányi, A., Muñoz-Sabater, J., et al. (2020). The ERA5 global reanalysis. *Quarterly Journal of the Royal Meteorological Society*, *146*(730), 1999–2049. https://doi.org/10.1002/qj.3803

Inch, K., Davidson, M., Masselink, G., & Russell, P. (2017). Observations of nearshore infragravity wave dynamics under high energy swell and wind-wave conditions. *Continental Shelf Research*, *138*, 19–31. https://doi.org/10.1016/j.csr.2017.02.010

Longuet-Higgins, M. S., & Stewart, R. W. (1962). Radiation stress and mass transport in gravity waves, with application to 'surf beats'. *Journal of Fluid Mechanics*, *3*(4), 481–504. https://doi.org/10.1017/s0022112062000877

Matsuba, Y., Shimozono, T., & Sato, S. (2020). Wave-breaking modulation by infragravity waves during an extreme typhoon. *PloS One*, *15*(4), 1–14. https://doi.org/10.1371/journal.pone.0231242

Munk, W., Snodgrass, F., & Gilbert, F. (1964). Long waves on the continental shelf: An experiment to separate trapped and leaky modes. *Journal of Fluid Mechanics*, *20*(4), 529–554. https://doi.org/10.1017/S0022112064001392

Neale, J., Harmon, N., & Srokosz, M. (2015). Source regions and reflection of infragravity waves offshore of the U.S. Pacific Northwest. *Journal of Geophysical Research: Oceans*, *9*(9), 6474–6491. https://doi.org/10.1002/2015jc010891

Okihiro, M., & Guza, R. T. (1995). Infragravity energy modulation by tides. *Journal of Geophysical Research*, *100*(C8), 16143. https://doi.org/10.1029/95jc01545

Okihiro, M., Guza, R. T., & Seymour, R. J. (1992). Bound infragravity waves. *Journal of Geophysical Research*, *97*(C7), 11453–11469. https://doi.org/10.1029/92jc00270

Okihiro, M., Guza, R. T., & Seymour, R. J. (1993). Excitation of seiche observed in a small harbor. *Journal of Geophysical Research*, *98*(C10), 18201–18211. https://doi.org/10.1029/93jc01760

Pomeroy, A., Lowe, R., Symonds, G., Van Dongeren, A., & Moore, C. (2012). The dynamics of infragravity wave transformation over a fringing reef. *Journal of Geophysical Research*, *11*(C11). https://doi.org/10.1029/2012jc008310

Rawat, A., Ardhuin, F., Ballu, V., Crawford, W., Corela, C., & Aucan, J. (2014). Infragravity waves across the oceans. *Geophysical Research Letters*, *11*(22), 7957–7963. https://doi.org/10.1002/2014gl061604

Reniers, A. J., Naporowski, R., Tissier, M. F. S., de Schipper, M. A., Akrish, G., & Rijnsdorp, D. P. (2021). North Sea infragravity wave observations. *Journal of Marine Science and Engineering*, *1*(2), 141. https://doi.org/10.3390/jmse9020141

Rhie, J., & Romanowicz, B. (2006). A study of the relation between ocean storms and the Earth's hum. *Geochemistry, Geophysics, Geosystems*, *7*(10). https://doi.org/10.1029/2006GC001274

Russell, P. E. (1993). Mechanisms for beach erosion during storms. *Continental Shelf Research*, *11*(11), 1243–1265. https://doi.org/10.1016/0278-4343(93)90051-x

Sheremet, A., Staples, T., Ardhuin, F., Suanez, S., & Fichaut, B. (2014). Observations of large infragravity-wave run-up at Banneg Island, France. *Geophysical Research Letters. 1*. 976–982. https://doi.org/10.1002/2013GL058880

Smit, P. B., Janssen, T. T., Herbers, T. H. C., Taira, T., & Romanowicz, B. A. (2018). Infragravity wave radiation across the shelf break. *Journal of Geophysical Research: Oceans*, *7*(7), 4483–4490. https://doi.org/10.1029/2018jc013986

Sugioka, H., Fukao, Y., & Kanazawa, T. (2010). Evidence for infragravity wave-tide resonance in deep oceans. *Nature Communications*, *1*(7), 1–7. https://doi.org/10.1038/ncomms1083

Symonds, G., Huntley, D. A., & Bowen, A. J. (1982). Two-dimensional surf beat: Long wave generation by a time-varying breakpoint. *Journal of Geophysical Research*, *87*(C1), 492–498. https://doi.org/10.1029/jc087ic01p00492

Thomson, J., Elgar, S., Raubenheimer, B., Herbers, T. H. C., & Guza, R. T. (2006). Tidal modulation of infragravity waves via nonlinear energy losses in the surfzone. *Geophysical Research Letters*, *33*(5). https://doi.org/10.1029/2005gl025514

Thotagamuwage, D. T., & Pattiaratchi, C. B. (2014). Influence of offshore topography on infragravity period oscillations in Two Rocks Marina, Western Australia. *Coastal Engineering*, *9*, 220–230. https://doi.org/10.1016/j.coastaleng.2014.05.011

Tonegawa, T., Fukao, Y., Shiobara, H., Sugioka, H., Ito, A., & Yamashita, M. (2018). Excitation location and seasonal variation of transoceanic infragravity waves observed at an absolute pressure gauge array. *Journal of Geophysical Research: Oceans*, *123*(1), 40–52. https://doi.org/10.1002/2017JC013488

Van der Molen, W., Monardez, P., & Van Dongeren, A. (2006). Numerical simulation of long-period waves and ship motions in Tomakomai port, Japan. *Coastal Engineering Journal*, *48*(1), 59–79. https://doi.org/10.1142/s0578563406001301

van der Molen, W., Scott, D., Taylor, D., & Elliott, T. (2016). Improvement of mooring configurations in Geraldton harbour. *Journal of Marine Science and Engineering*, *4*(1), 1–20. https://doi.org/10.3390/jmse4010003

Van Dongeren, A., Battjes, J., Janssen, T., van Noorloos, J., Steenhauer, K., Steenbergen, G., & Reniers, A. (2007). Shoaling and shoreline dissipation of low-frequency waves. *Journal of Geophysical Research*, *2*(C2). https://doi.org/10.1029/2006jc003701

Van Thiel de Vries, J. S. M., Van Gent, M. R. A., Walstra, D. J. R., & Reniers, A. J. H. M. (2008). Analysis of dune erosion processes in large-scale flume experiments. *Coastal Engineering*, *12*(12), 1028–1040. https://doi.org/10.1016/j.coastaleng.2008.04.004

Vrećica, T., Soffer, R., & Toledo, Y. (2019). Infragravity wave generation by wind gusts. *Geophysical Research Letters*, *8*(16), 9728–9738. https://doi.org/10.1029/2019GL084241

Webb, S. C. (2007). The Earth's 'hum' is driven by ocean waves over the continental shelves. *Nature*, *445*(7129), 754–756. https://doi.org/10.1038/nature05536

Webb, S. C., Zhang, X., & Crawford, W. (1991). Infragravity waves in the deep ocean. *Journal of Geophysical Research*, *96*(C2), 2723–2736. https://doi.org/10.1029/90jc02212

Zijlema, M., Van Vledder, G. P., & Holthuijsen, L. H. (2012). Bottom friction and wind drag for wave models. *Coastal Engineering*, *65*, 19–26. https://doi.org/10.1016/j.coastaleng.2012.03.002